Proceedings of the ASME 2013 Dynamic Systems and Control Conference
DSCC2013
October 21-23, 2013, Palo Alto, California, USA

DSCC2013-3942

REGULATION OF 3D HUMAN ARM IMPEDANCE THROUGH MUSCLE CO-CONTRACTION

Harshil Patel, Gerald O'Neill and Panagiotis Artemiadis
Human-Oriented Robotics and Control Lab
School for Engineering of Matter, Transport and Energy
Arizona State University
Tempe, AZ 85287
Email: {hpatel5, goneill, panagiotis.artemiadis}@asu.edu

ABSTRACT

Humans have the inherent ability of performing highly dexterous and skillful tasks with their arms, involving maintenance of posture, movement, and interaction with the environment. The latter requires the human to control the dynamic characteristics of the upper limb musculoskeletal system. These characteristics are quantitatively represented by inertia, damping, and stiffness, which are measures of mechanical impedance. Many previous studies have shown that arm posture is a dominant factor in determining the end point impedance on a horizontal (transverse) plane. This paper presents the characterization of the end point impedance of the human arm in three-dimensional space. Moreover, it models the regulation of the arm impedance with respect to various levels of muscle co-contraction. The characterization is made by route of experimental trials where human subjects maintained arm posture while their arms were perturbed by a robot arm. Furthermore, the subjects were asked to control the level of their arm muscles' co-contraction, using visual feedback of their muscles' activation, in order to investigate the effect of this muscle co-contraction on the arm impedance. The results of this study show a very interesting, anisotropic increase of arm stiffness due to muscle co-contraction. These results could lead to very useful conclusions about the human's arm biomechanics, as well as many implications for human motor control-specifically the control of arm impedance through muscle co-contraction.

INTRODUCTION

The wide range of applications involving physical interaction of robots with humans has received increased attention in the last few decades. Since the late 80's, there has been a substantial amount of interest in measuring human arm two dimensional (2D) end-point stiffness characteristics, where the arm is supported and constrained to movement within a horizontal (transverse) plane. A perturbation method for measuring hand stiffness was developed by using a manipulandum to displace the subject's hand during maintenance of a given posture in [1]. Stiffness values were represented both numerically and as ellipses (graphically). These showed that the human musculo-skeletal system has spring like properties that enable posture stabilization and interaction with the environment.

The perturbation method for estimating arm stiffness has been used by many other studies as well [2–5]. In [6] and [7], the perturbation method was extended to include measurement of other dynamic components: inertia and damping in addition to stiffness. The first attempt to characterize arm impedance in three-dimensional (3D) space was described in [8]. However the stochastic methods used were not able to provide an insight into the neuromuscular system and its interaction with the environment.

Although most of the past studies have focused on perturbations during maintained hand posture, there are only a few studies that focused on the effect of muscle activation on the arm stiffness- again only on the horizontal (transverse) plane [2,9,10]. Since every-day tasks involve movement of the upper arm in the 3D space, the characterization of human arm impedance in this space and the contribution of muscle co-contraction towards changing these characteristics is significant.

In this paper, a systematic method for characterizing human arm impedance in the 3D space and its regulation through muscle co-contraction is presented. A 7 degrees-of-freedom (DoFs)

 Copyright © 2013 by ASME

robot arm is used to impose motion to, and measure interaction forces from, a human subject's arm. The subject's arm is appropriately coupled to the robot's end-effector and is perturbed along the three axes starting from 7 different points, each corresponding to 7 different arm configuration in 3D space. The perturbations follow a specifically programmed trajectory in order to study the dynamic behavior of the subject's arm. All the perturbations are repeated in four phases, each with a different level of muscle co-contraction. A simplified linear model for impedance is used to characterize inertia, damping and stiffness using measured motion and force data for the 4 cases of muscle co-contraction. The stiffness characteristics are described using ellipsoids, and the effect of arm configuration and muscle co-contraction to the stiffness ellipsoids is investigated.

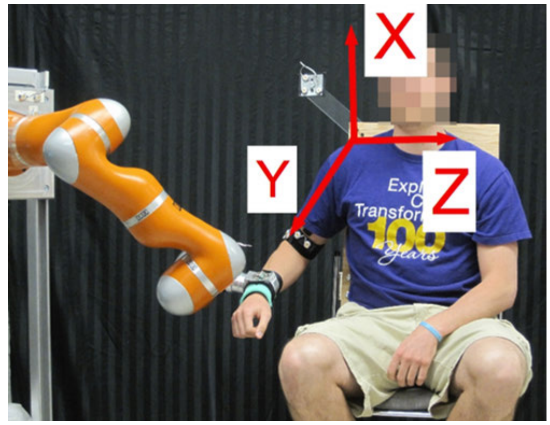

Figure 1. Experimental setup: The robot arm is interfaced with the subject's forearm through the mechanical coupling attached at the end-effector. Position tracking sensors are placed adjacent to the robot base and subject's shoulder defining two reference systems. EMG electrodes are placed on 6 muscles of the shoulder and elbow. Chair straps are not shown in the picture, but they were used during the experiments.

MATERIALS AND METHODS
Apparatus

The subjects were seated on a chair placed next to a 7-DoF robot arm (LWR4+, KUKA). They were strapped to the chair and their right arm was coupled to the robot arm via a mechanical coupling, attached to the end-effector of the robot arm as shown in Fig.1. The mechanical coupling is designed such that it allows no axial or rotational movement of the lower arm inside it, since it is attached to the human forearm close to the wrist [11]. The coupling insured that there was no kinematic redundancy in the subject's arm for any configuration. The mechanical coupling is capable of transmitting forces and torques in all directions between the robot and the coupled human arm. The robot arm position and force measurement accuracy is $0.01mm$ and $0.01N$ respectively, which are sufficient for this experiment. An active motion capture system was used (3D Investigator, NDI Inc) to track the motion of the arm, as well as compute the human arm configuration. Two reference systems were defined; one at the mounting plate of the robot arm $\langle X_B, Y_B, Z_B \rangle$, and the other at the shoulder of the human subject $\langle X, Y, Z \rangle$. The latter is defined so that the subject's torso coincides with the X-Z plane and the vector joining the shoulders is parallel to the Z-axis. Finally, the X axis is vertically oriented as shown in Fig.1.

Muscle activation was measured through wireless surface electromyography (EMG) electrodes (Trigno Wireless, Delsys). Since the focus is arm impedance, and the coupling is on the forearm, the muscles that contribute to shoulder and elbow impedance were recorded. The muscles we recorded from are: Anterior Deltoid, Posterior Deltoid, Pectoralis Major, Trapezius, Biceps Brachii and Triceps long.

Procedure and Tasks

Four subjects, all male ranging in age from 20 to 26 years, three of them right handed and one left handed, participated in this experiment. As explained above, the subjects were strapped onto a seat placed next to the robot arm. Seven different end-effector poses (position and orientation) in the robot workspace were selected. With the subject strapped in the same position on the chair and their right hand coupled to the end-effector, each of these start points $S^{(i)} : i = 1, 2, .., 7$ corresponded to a specific configuration of the subject's arm. The seven arm configurations tested spanned a wide range of arm positions in 3D space, as shown in Fig. 2. The robot was controlled to impose perturbations in 18 different directions in 3D space. This was done by controlling the robot to move to 18 equally-spaced points $P_j^{(i)}$, $j = 1, \ldots, 18$ that lie on a sphere with a center of the corresponding $S^{(i)}$ point, and a radius of $8mm$. The motion of the robot from $S^{(i)}$ to one of the 18 $P_j^{(i)}$ points lasted $100ms$, and corresponded to the robot-induced perturbation to the human arm. Once the robot arrives at $P_j^{(i)}$, it remains stationary for $500ms$ and then returns back to $S^{(i)}$. After a resting phase of $1s$, the robot is commanded to reach the next $P_j^{(i)}$ point, and the procedure is repeated for all the 18 $P_j^{(i)}$ points.

The trajectory of the robot motion along each axis was designed using a 3rd order polynomial function. The trajectories were planned such that the orientation angles of the robot end-effector (roll, pitch, yaw) remained the same as those of the corresponding start points. The pseudo-inverse Jacobian method for solving the inverse kinematics of the robot arm was used offline [12]. Once the robot joint angle trajectories were computed, they were fed to the robot arm controller. The robot provided feedback of the joint angles, as well as end-effector forces at a frequency of $1000Hz$.

Prior to performing the experiment, the subjects were asked to co-contract their arm muscles to their maximum ability, while their arm was in one of the 7 configurations selected (configuration 5). EMG signals were recorded from the six muscles mentioned above and sampled at a frequency of $1000Hz$. The signals were then full-wave rectified and low-pass filtered (2nd

Copyright © 2013 by ASME

order Butterworth filter, cut-off frequency of 8 Hz). The processed signals $e_m, m = 1, \ldots, 6$ were stored, and the maximum values for each muscle $e_{m,\max}$ were recorded to be used as a normalization factor for the experiments. During the perturbation experiments the total co-contraction index C was computed in real-time based on the individual muscle normalized activation level with respect to their maximum activation level $e_{m,\max}$. Therefore, the co-contraction index was given by:

$$C = \frac{1}{6} \sum_{m=1}^{6} \frac{e_m}{e_{m,\max}} \tag{1}$$

The robot-induced perturbation experiments were divided into four phases. In each phase, the subject was asked to maintain a certain co-contraction level of his/her muscles. The robot-induced perturbations were identical across the four phases. The co-contraction index C was computed in real-time based on the muscles' activation, and was displayed to the subject in the form of a bar graph, as shown in Fig. 3. The visual display was shown on a monitor placed in front of the subject, and was updated at a frequency of $1000Hz$. The levels of co-contraction asked of the subjects to maintain were 0%, 50%, 75% and 100% for the four phases respectively. For each of the 7 arm configurations, the robot perturbation phase was divided into three sets of 6 perturbations each, thereby providing enough time for the subject to relax his/her muscles and limiting possible muscle fatigue.

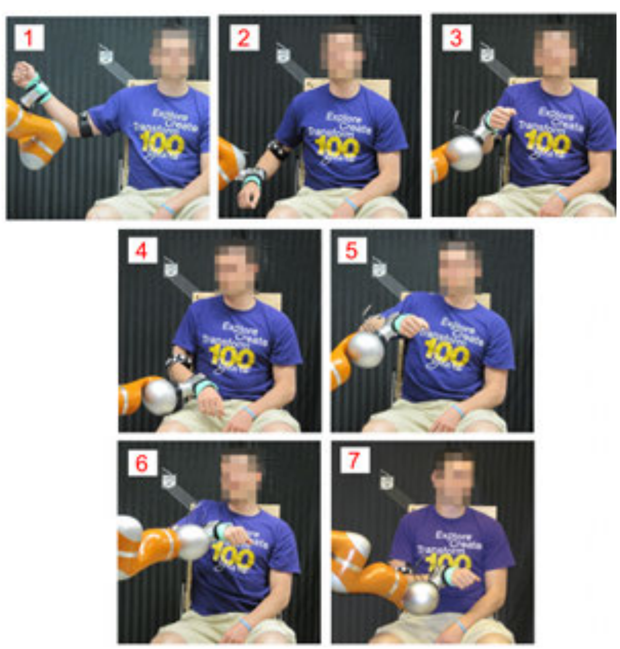

Figure 2. The 7 configurations of the arm used.

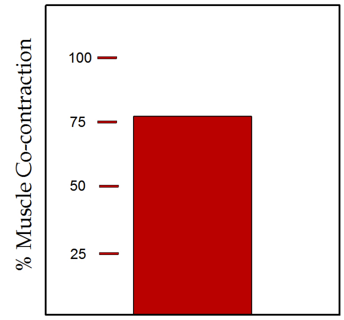

Figure 3. Visual display indicating the muscle co-contraction index.

Data Processing

As explained earlier, the goal of the study is to investigate how the arm impedance changes as a function of muscle co-contraction. The arm impedance characteristics - inertia, damping and stiffness - are characterized using a linear model describing the relationship between measured restoring forces and position of the arm.

In the experiment, the arm is coupled to the end-effector of the robot arm via the mechanical coupling. The position of the end point of the arm, a point in the forearm, was defined as the center point of the cylindrical housing of the mechanical coupling. Since the coupling was attached to the robot arm, the 3D position of this point was tracked at each instance through the robot joint angles after applying the forward kinematic equations of the robot arm. Therefore, all the motion profiles and end-effector forces were obtained with respect to the robot base reference system $\langle X_R, Y_R, Z_R \rangle$. Using homogeneous transformation between the robot and the robot mounting plate reference system $\langle X_B, Y_B, Z_B \rangle$, the position of the human end-point, and the interaction forces, were computed with respect to the human-centered reference frame $\langle X, Y, Z \rangle$

Impedance estimation

The force and motion profiles of interest, i.e. during the $100ms$ robot-induced perturbations, were extracted for processing. The initial values of forces in all directions were first subtracted from the subsequent force profiles. This ensured that any kind of sensor offset or gravitational forces due to weight of the arm didn't affect the restoring force measurements. Since length and duration of the perturbations was very small, the model of the end point impedance can be expressed by the following equation:

$$\mathbf{F} = \mathbf{I}\ddot{\mathbf{X}} + \mathbf{B}\dot{\mathbf{X}} + \mathbf{K}\mathbf{X} \tag{2}$$

where $\mathbf{I}$, $\mathbf{B}$ and $\mathbf{K}$ represent the 3×3 arm inertia, damping and stiffness matrices respectively. $\ddot{\mathbf{X}}$, $\dot{\mathbf{X}}$ and $\mathbf{X}$ are the 3D acceleration, velocity and displacement vectors respectively, while $\mathbf{F}$ is the 3D vector of restoring forces. All variables are expressed with respect to the human-centered reference system $\langle X, Y, Z \rangle$.

Copyright © 2013 by ASME

Equation (2) can be re-written in a parameter identification form as shown below:

$$\mathbf{F} = \mathbf{P}\mathbf{y} \tag{3}$$

where $\mathbf{F} = [F_x \quad F_y \quad F_z]^T$, $\mathbf{y} = [\ddot{\mathbf{X}}^\mathbf{T} \quad \dot{\mathbf{X}}^\mathbf{T} \quad \mathbf{X}^\mathbf{T}]^T$ and $\mathbf{P}$ is a 3×9 impedance matrix to be identified, given by

$$\mathbf{P} = [\mathbf{I} \quad \mathbf{B} \quad \mathbf{K}] \tag{4}$$

where $\mathbf{I}$ is the inertia matrix defined by

$$\mathbf{I} = \begin{bmatrix} I_{xx} & I_{xy} & I_{xz} \\ I_{yx} & I_{yy} & I_{yz} \\ I_{zx} & I_{zy} & I_{zz} \end{bmatrix} \tag{5}$$

$\mathbf{B}$ is the damping matrix defined by

$$\mathbf{B} = \begin{bmatrix} B_{xx} & B_{xy} & B_{xz} \\ B_{yx} & B_{yy} & B_{yz} \\ B_{zx} & B_{zy} & B_{zz} \end{bmatrix} \tag{6}$$

$\mathbf{K}$ is the stiffness matrix defined by

$$\mathbf{K} = \begin{bmatrix} K_{xx} & K_{xy} & K_{xz} \\ K_{yx} & K_{yy} & K_{yz} \\ K_{zx} & K_{zy} & K_{zz} \end{bmatrix}. \tag{7}$$

Using n number of data points for restoring force and position measurements collected from the experiments, the impedance matrix P was computed using linear regression method given by the following:

$$\mathbf{P} = \mathbf{F}_N \mathbf{Y}_N^\dagger \tag{8}$$

where $\mathbf{Y}_N^\dagger$ is the left pseudo-inverse matrix of $\mathbf{Y}_N$. $\mathbf{F}_N$ and $\mathbf{Y}_N$ were computed by concatenating n instances of $\mathbf{F}$ and $\mathbf{y}$ respectively as follows:

$$\mathbf{F}_N = [\mathbf{F}_1 \cdots \mathbf{F}_n] \tag{9}$$

$$\mathbf{Y}_N = [\mathbf{Y}_1 \cdots \mathbf{Y}_n] \tag{10}$$

The impedance matrices $\mathbf{I}$, $\mathbf{B}$ and $\mathbf{K}$ were separated into symmetric and antisymmetric matrix components. Generally any 3×3 matrix $\mathbf{Z}$ can be separated into the symmetric $Z^{(S)}$ and anti-symmetric component $Z^{(A)}$ as follows:

$$\mathbf{Z} = \begin{bmatrix} Z_{xx} & Z_{xy} & Z_{xz} \\ Z_{yx} & Z_{yy} & Z_{yz} \\ Z_{zx} & Z_{zy} & Z_{zz} \end{bmatrix} = \mathbf{Z}^{(S)} + \mathbf{Z}^{(A)} \tag{11}$$

where

$$\begin{aligned} \mathbf{Z}^{(S)} &= \frac{1}{2}(\mathbf{Z} + \mathbf{Z}^T) \\ \mathbf{Z}^{(A)} &= \frac{1}{2}(\mathbf{Z} - \mathbf{Z}^T) \end{aligned} \tag{12}$$

Finally, if $f(x,y,z)$ is a differentiable, non-linear function of the position of the arm end-point, where x,y,z is the position of the end point in 3D space, it is possible to express the end point impedance of the arm as a differential operator that relates small variations of force (dF_x, dF_y, dF_z) to small displacements (dx, dy, dz), i.e.

$$\begin{aligned} dF_x &= \left(\frac{\partial F_x}{\partial x}\right) dx + \left(\frac{\partial F_x}{\partial y}\right) dy + \left(\frac{\partial F_x}{\partial z}\right) dz \\ &= Z_x x d_x + Z_x y d_y + Z_x z d_z \\ dF_y &= \left(\frac{\partial F_y}{\partial x}\right) dx + \left(\frac{\partial F_y}{\partial y}\right) dy + \left(\frac{\partial F_y}{\partial z}\right) dz \\ &= Z_y x d_x + Z_y y d_y + Z_y z d_z \\ dF_z &= \left(\frac{\partial F_z}{\partial x}\right) dx + \left(\frac{\partial F_z}{\partial y}\right) dy + \left(\frac{\partial F_z}{\partial z}\right) dz \\ &= Z_z x d_x + Z_z y d_y + Z_y z d_z \end{aligned} \tag{13}$$

The above equation holds true for small displacements. Therefore the physical meaning of the symmetric impedance component is that the force field $f(x,y,z)$ is conservative. And the anti-symmetric component represents the curl of the force field mainly generated by the subjects' hand [1].

Impedance representation

An ellipsoid centered at the origin is represented by the following equation:

$$a_{11}x^2 + a_{22}y^2 + a_{33}z^2 + 2a_{12}xy + 2a_{13}xz + 2a_{23}yz = 1 \tag{14}$$

where $a_{11}, a_{22}, a_{33}, a_{12}, a_{13}, a_{23}$ are elements of a symmetric 3×3 matrix $\mathbf{A}$, i.e

$$\mathbf{A} = \begin{bmatrix} a_{11} & a_{12} & a_{13} \\ a_{12} & a_{22} & a_{23} \\ a_{13} & a_{23} & a_{33} \end{bmatrix} \tag{15}$$

Copyright © 2013 by ASME

The principle axes of the ellipsoid $\mathbf{x}^{(1)}, \mathbf{x}^{(2)}, \mathbf{x}^{(3)} \in \mathbb{R}^3$ are the eigenvectors of the matrix $\mathbf{A}$, and they are all orthogonal to each other. These eigenvectors essentially define the principal reference system of the ellipsoid. Let α,β and γ be the yaw, pitch and roll angles that define the orientation of the principle reference system of the ellipsoid, with respect to the base reference system. The rotation matrix describing the ellipsoid principal reference system with respect to the base reference system is given by:

$$\mathbf{R}(\alpha,\beta,\gamma) = \mathbf{R_z}(\alpha)\mathbf{R_y}(\beta)\mathbf{R_x}(\gamma) \tag{16}$$

Solving (16) for the α, β and γ orientation angles,

$$\begin{aligned} \alpha &= tan^{-1}\left(\frac{r_{21}}{r_{11}}\right) \\ \beta &= tan^{-1}\left(\frac{-r_{31}}{\sqrt{r_{32}^2 + r_{33}^2}}\right) \\ \gamma &= tan^{-1}\left(\frac{r_{32}}{r_{33}}\right) \end{aligned} \tag{17}$$

where $[\mathbf{x^{(1)}} \quad \mathbf{x^{(2)}} \quad \mathbf{x^{(3)}}] = \begin{bmatrix} r_{11} & r_{12} & r_{13} \\ r_{12} & r_{22} & r_{23} \\ r_{13} & r_{23} & r_{33} \end{bmatrix}$.

The equatorial radii a, b and the polar radius c, along the principal axes $\mathbf{x}^{(1)}, \mathbf{x}^{(2)}$ and $\mathbf{x}^{(3)}$ respectively of the ellipsoid are given by: $a = \frac{1}{\sqrt{\lambda_1}}$, $b = \frac{1}{\sqrt{\lambda_2}}$, $c = \frac{1}{\sqrt{\lambda_3}}$ where λ_1, λ_2, λ_3 are the eigenvalues of the matrix $\mathbf{A}$.

Based on all of the above, the symmetric components of the stiffness matrices $\mathbf{K}^{(S)}$ across all configurations, were represented by ellipsoids with center at starting points $(S^{(i)}, i = 1,2,..,7)$, radii along the individual principal axes and orientation defined above. It must be noted that the ellipsoids plotted represent the end-point stiffness at each configuration, i.e. the longer the radius in a particular direction, the higher the stiffness in that direction.

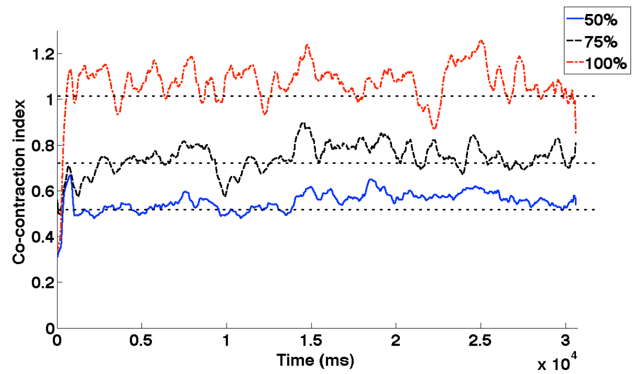

Figure 4. Co-contraction index C for three muscle co-contraction levels 50%, 75% and 100%. A similar trend of maintaining the co-contraction index was seen for all the subjects.

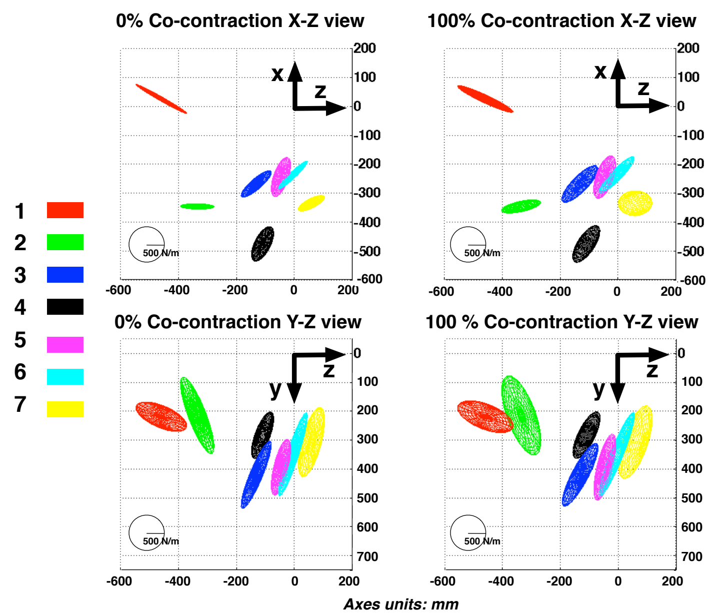

Figure 5. Stiffness ellipsoids for a representative subject. Check Fig. 1 and 2 for axes and configurations. The 7 different configurations are color-coded on the left.

RESULTS
Co-Contraction Index

Before analyzing the impedance characteristics identified for the various levels of muscle co-contraction, it is worth investigating the ability of the human subjects to control their muscles' activation, based on the visual feedback of the co-contraction index introduced above. Fig. 4 shows the co-contraction index as calculated in three trials, in which the subject was instructed to maintain it at 50%, 75% and 100% level respectively. It can be seen that the subject was able to maintain the specific level of muscle co-contraction in each phase. These indexes were seen to slightly vary across the 7 configurations indicating that the ability to co-contract the muscles to the specific level of co-contraction was different for different arm configurations. However, we chose to define the co-contraction index with respect to maximum voluntary co-contraction in a *single* arm configuration. Although we could use maximum voluntary co-contraction for each configuration tested, we decided to use only one in order to have a more general idea of the muscle co-contraction level, that could generalize across configurations. This would allow further investigation of the ability of muscles to co-contract without being limited on the arm configuration. Configuration 5 was selected because it was approximately in the mid-range of the 3D arm workspace we used. However, further analysis on this issue is out of the scope of this paper.

Copyright © 2013 by ASME

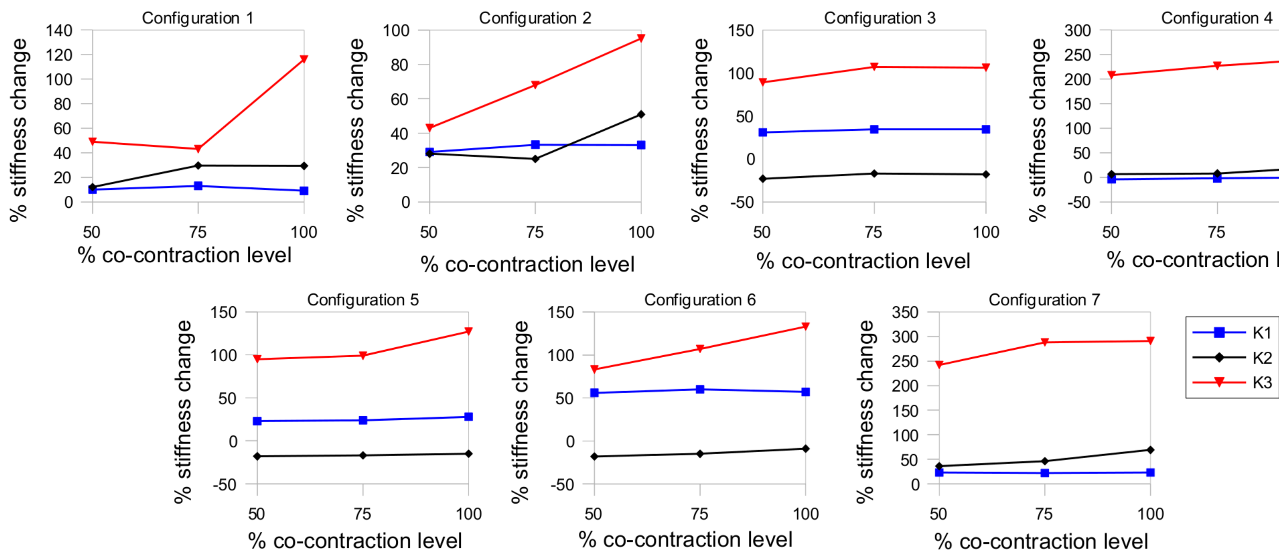

Figure 6. Increase of arm stiffness along the primary, secondary, and tertiary axes of the ellipsoids for the different co-contraction levels.

Impedance matrices

The impedance matrices I, B and K for each of the arm configurations were identified and separated into the symmetric and antisymmetric components as described in the previous section. It was observed that the restoring forces due to inertia (I) and damping (B) were very small compared to the ones due to arm stiffness, especially in the cases involving muscle co-contraction. For that reason, it is not certain that they were accurately identified using the least-squares equation. Moreover, we don't expect the inertia of the arm to vary for different muscle co-contraction levels, and there is no evidence from the literature that damping would also change with muscle co-contraction, especially given isometric conditions we investigate here.Therefore, following directions also provided by the literature [1,3], we decided to analyze only the effects of co-contraction on arm stiffness.

The diagonal elements of the identified arm stiffness $\overline{K}_{xx}$, $\overline{K}_{yy}$, $\overline{K}_{zz}$, averaged across all subjects, are listed in Tables 1, 2, 3, 4 for the different co-contraction levels 0%, 50%, 75% and 100% respectively. Moreover, the maximum of all off-diagonal elements of the anti-symmetric components are also listed. Finally, as discussed above, the stiffness was represented as an ellipsoid in 3D space. The length of each of the primary, secondary, and tertiary axes of each ellipsoid is also listed in those tables, as $\overline{K}_1$, $\overline{K}_2$ and $\overline{K}_3$ respectively. Fig. 5 shows the stiffness ellipsoids, for one of the subjects, across all 7 configurations, for 0% and 100% muscle co-contraction.

The results show that there is a significant effect of both the arm configuration and the muscle activation level on arm stiffness. The range of stiffness values we estimated is very close to these reported in the literature for the 2D case [2–5]. Moreover, the antisymmetric components of the stiffness were observed to be much lower then the symmetric components, which agrees with the literature for planar arm configurations [1]. Of most importance, however, is the relationship between the stiffness ellipsoids and muscle co-contraction. Fig. 6 shows the percent increase of arm stiffness along the primary, secondary, and tertiary axes of the ellipsoids for the different co-contraction levels. Moreover, Table 5 shows the rotation of the stiffness ellipsoids due to muscle co-contraction. More specifically, Table 5 reports the angle difference of each of the ellipsoid axes, for the 100% co-contraction case with respect the 0% case. Reported values are averaged across subjects. As it can be seen for Tables 1, 2, 3 and 4, as well as Fig. 6, muscle co-contraction *enlarges* the stiffness ellipsoid primarily along the tertiary axis. The ellipsoids didn't significantly change along the principal and secondary axes, with a maximum overall change of 50% observed only in a couple of configurations. In terms of rotation of the ellipsoids, a 100% muscle co-contraction rotates the secondary and tertiary axes by 24.2° in average, compared to the 0% co-contraction case, while for only 8.5° in average in the case of the primary axis. From these observations we can conclude that muscle co-contraction induces an anisotropic change of the arm stiffness, affecting primarily the secondary and tertiary axes of the ellipsoids, and not the primary axis. A possible explanation of this phenomenon is the way individual muscles contribute to this change of the overall arm stiffness, which is a function of both the configuration of the arm, as well as the properties of each muscle independently. A further investigation of the geometry of the musculoskeletal models, as well as the contribution of each muscle to the overall arm Cartesian stiffness should be conducted. However, it is worth noting that the results are very consistent across subjects, which proves the validity of the proposed method, as well as the possibly groundbreaking importance of this study in the study of the biomechanics of the human upper limb, with a plethora of implications for the EMG-based control of orthotic devices.

Copyright © 2013 by ASME

CONCLUSIONS

In this paper, a systematic method for characterizing the human arm impedance in the 3D space and its regulation through muscle co-contraction is presented. The proposed method is based on robot-induced perturbations in posture maintenance scenarios, however it introduces control of muscle co-contraction level by the human subject, through visual feedback. A simplified linear model for impedance is used to characterize arm stiffness using the measured motion and force data for 4 cases of muscle co-contraction (0%, 50%, 75% and 100%). The stiffness characteristics are described using ellipsoids, and the effect of arm configuration and muscle co-contraction on the stiffness ellipsoids is investigated.

The main novelty of this paper is that it succeeds in characterizing human arm impedance in 3D space, while investigating the control humans have over the arm stiffness using muscle co-contraction. The method was applied to 4 human subjects, across whom the results were very consistent, which proves the validity of the proposed method. Based on the results, we can conclude that muscle co-contraction induces an anisotropic change of the arm stiffness, affecting primarily the secondary and tertiary axes of the ellipsoids, and not the primary axis. A definite explanation of this phenomenon requires further investigation, including a musculoskeletal model of the arm in order to quantify the role of the individual muscles in the overall end-point Cartesian impedance. This study is of possible groundbreaking importance for the field of biomechanics of the human upper limb, with a plethora of implications for EMG-based control of robots that physically interact with humans.

REFERENCES

[1] Mussa-Ivaldi, F. A., Hogan, N., and Bizzi, E., 1985. "Neural, mechanical, and geometric factors subserving arm posture in humans". *J Neurosci*, pp. 2732–2743.

[2] Tsuji, T., and Kaneko, M., 1996. "Estimation and modeling of human hand impedance during isometric muscle contraction". *ASME Dynamics Systems and Control Division,* **58**, pp. 575–582.

[3] Burdet, E., Osu, R., Franklin, D. W., Yoshioka, T., Milner, T. E., and Kawato, M., 2000. "A method for measuring endpoint stiffness during multi-joint arm movements". *Journal of Biomechanics,* **33**, pp. 1705–1709.

[4] Perreault, E. J., Kirsch, R. F., and Crago, P. E., 2001. "Effects of voluntary force generation, on the elastic components of endpoint stiffness". *Exp Brain Res,* **141**, pp. 312–323.

[5] Perreault, E. J., Kirsch, R. F., and Crago, P. E., 2002. "Voluntary control of static endpoint stiffness during force regulation tasks". *J Neurophysiol,* **87**, pp. 2808–2816.

[6] Dolan, J. M., Friedman, M. B., and Nagurka, M. L., 1993. "Dynamic and loaded impedance components in the maintenance of human arm posture". *IEEE Trans Systems, Man, and Cybernetics,* **23**, pp. 698–709.

[7] Tsuji, T., Morasso, P. G., Goto, K., and Ito, K., 1995. "Human hand impedance characteristics during maintained posture". *Biol Cybern*, pp. 475–485.

[8] Pierre, M. C., and Kirsch, R. F., 2002. "Measuring dynamic characteristics of the human arm in three dimensional space". *Proceedings of the Second Joint EMBS/BMES Conference,* **3**, pp. 2558–2560.

[9] Flash, T., and Mussa-Ivaldi, F. A., 1990. "Human arm stiffness characteristics during the maintenance of posture". *Exp Brain Res*, pp. 315–326.

[10] Osu, R., and Gomi, H., 1999. "Multijoint muscle regulation mechanisms examined by measured human arm stiffness and EMG signals". *J Neurophysiol,* **81**, pp. 1458–1468.

[11] O'Neill, G., Patel, H., and Artemiadis, P., 2013 (submitted). "An intrinsically safe mechanism for physically coupling humans with robots". *IEEE Int. Conf. on Rehabilitation Robotics*.

[12] Sciavicco, L., and Siciliano, B., 1996. *Modeling and control of robot manipulators*. McGraw-Hill.

Copyright © 2013 by ASME

Table 1. Arm stiffness characteristics for 0% co-contraction, averaged across all subjects.

Configuration #	$\overline{K}_{xx}$ (N/m)	$\overline{K}_{yy}$ (N/m)	$\overline{K}_{zz}$ (N/m)	$\overline{K}_{max_A}$ (N/m)	$\overline{K}_1$ (N/m)	$\overline{K}_2$ (N/m)	$\overline{K}_3$ (N/m)
1	580.7	1082.0	1439.5	348.7	2202.1	711.5	188.7
2	269.6	2405.1	873.4	507.2	2740.1	661.3	146.6
3	455.8	2357.3	739.1	370.3	2807.6	476.6	268.1
4	862.8	1735.2	583.1	136.8	2046.6	663.4	471.1
5	667.3	2158.9	509.2	344.5	2550.1	484.3	301.1
6	458.7	2904.9	654.1	163.5	3264.9	505.1	247.7
7	684.9	2314.8	764.3	401.4	2549.9	845.9	368.3

Table 2. Arm stiffness characteristics for 50% co-contraction, averaged across all subjects.

Configuration #	$\overline{K}_{xx}$ (N/m)	$\overline{K}_{yy}$ (N/m)	$\overline{K}_{zz}$ (N/m)	$\overline{K}_{max_A}$ (N/m)	$\overline{K}_1$ (N/m)	$\overline{K}_2$ (N/m)	$\overline{K}_3$ (N/m)
1	651.1	1177.1	1674.6	290.5	2421.0	799.6	282.2
2	559.9	2435.1	1021.5	492.4	2841.2	910.3	265.0
3	524.1	2406.1	829.1	378.8	2887.5	541.6	330.2
4	973.4	1766.3	654.6	113.3	2108.3	747.3	538.7
5	799.4	2243.3	613.4	356.6	2725.4	574.0	356.7
6	630.2	2927.0	775.6	213.1	3438.4	570.0	324.2
7	944.5	2432.1	900.8	375.1	2721.6	955.0	600.4

Table 3. Arm stiffness characteristics for 75% co-contraction, averaged across all subjects.

Configuration #	$\overline{K}_{xx}$ (N/m)	$\overline{K}_{yy}$ (N/m)	$\overline{K}_{zz}$ (N/m)	$\overline{K}_{max_A}$ (N/m)	$\overline{K}_1$ (N/m)	$\overline{K}_2$ (N/m)	$\overline{K}_3$ (N/m)
1	451.8	1078.3	2144.3	293.3	2499.6	921.8	253.0
2	620.5	2516.1	1004.6	475.6	2928.7	894.3	318.1
3	602.7	2424.6	877.3	337.3	2949.5	585.7	369.4
4	987.5	1773.2	709.7	122.9	2132.0	755.6	582.6
5	790.2	2278.1	608.3	354.4	2731.3	582.1	363.5
6	676.8	2968.0	826.7	219.1	3518.9	590.9	361.0
7	1026.1	2441.9	943.2	350.8	2701.0	1022.4	686.9

Copyright © 2013 by ASME

Table 4. Arm stiffness characteristics for 100% co-contraction, averaged across all subjects.

Configuration #	$\overline{K}_{xx}$ (N/m)	$\overline{K}_{yy}$ (N/m)	$\overline{K}_{zz}$ (N/m)	$\overline{K}_{max_A}$ (N/m)	$\overline{K}_1$ (N/m)	$\overline{K}_2$ (N/m)	$\overline{K}_3$ (N/m)
1	595.9	1149.8	1985.1	318.1	2406.5	910.1	414.2
2	718.9	2502.8	1148.4	470.7	2924.1	1090.4	355.2
3	641.9	2423.5	844.2	334.4	2955.3	579.3	374.0
4	1076.9	1830.9	728.3	114.2	2182.5	845.5	608.0
5	831.3	2371.6	660.6	379.3	2827.8	642.2	393.4
6	725.3	3002.6	788.4	232.1	3471.0	627.6	417.7
7	1167.8	2476.4	915.5	339.6	2701.0	1191.2	667.5

Table 5. Rotation angles of the primary, secondary, and tertiary axes of of stiffness ellipsoids from 0% to 100% co-contraction.

Configuration #	$\Delta\theta_1(^\circ)$	$\Delta\theta_2(^\circ)$	$\Delta\theta_2(^\circ)$
1	26.0	32.2	27.7
2	6.6	12.4	14.8
3	5.7	25.8	27.3
4	6.7	35.2	35.1
5	4.9	16.5	16.2
6	3.7	23.6	23.8
7	6.5	23.7	24.5

Copyright © 2013 by ASME